*minerals*

MDPI

*Article*

# Transport Model of Rare Earth Elements in Weathering Crusts during Electrokinetic Mining

**Gaofeng Wang [1,2,3], Bowen Ling [4,5], Xiaoliang Liang [1,2,3], Jie Xu [1,2,3], Shichang Kang [1,2,3], Jingming Wei [1,2,3], Wei Tan [1,2,3], Runliang Zhu [1,2,3], Jianxi Zhu [1,2,3,*] and Hongping He [1,2,3]**

1 CAS Key Laboratory of Mineralogy and Metallogeny/Guangdong Provincial Key Laboratory of Mineral Physics and Material, Guangzhou Institute of Geochemistry, Chinese Academy of Sciences, Guangzhou 510640, China; wanggaofeng@gig.ac.cn (G.W.); liangxl@gig.ac.cn (X.L.); xujie777@gig.ac.cn (J.X.); kangshichang@gig.ac.cn (S.K.); weijm@gig.ac.cn (J.W.); tanwei@gig.ac.cn (W.T.); zhurl@gig.ac.cn (R.Z.); hehp@gig.ac.cn (H.H.)
2 CAS Center for Excellence in Deep Earth Science, Guangzhou 510640, China
3 University of Chinese Academy of Sciences, Beijing 100049, China
4 Key Laboratory for Mechanics in Fluid Solid Coupling Systems, Institute of Mechanics, Chinese Academy of Sciences, Beijing 100190, China; lingbowen@imech.ac.cn
5 School of Engineering Science, University of Chinese Academy of Sciences, Beijing 100049, China
* Correspondence: zhujx@gig.ac.cn

**Abstract:** Electrokinetic mining (EKM) is a novel method for rare earth element (REE) mining that can achieve green and efficient recovery of REEs. However, as yet, there is no accurate model for describing the electrokinetic transport of REEs in weathering crusts, and this hinders the wider application of EKM. The conventional model fails to capture the microscale transport physics occurring in the nanochannels that exist ubiquitously in weathering crusts. Consequently, the existing models cannot distinguish the mobilities of different REEs. Here, we report a new model for a more faithful description of the electrokinetic transport of REEs in weathering crusts that considers the ionic size, which has previously been neglected. We reveal that the electrokinetic transport of heavy REEs (HREEs) is faster than that of light REEs (LREEs) in weathering crusts, which is contrary to the predictions of conventional models. Our model was validated experimentally by measurements of the electrokinetic transport of two LREEs (La and Sm) and an HREE (Er) in weathering crusts. The speed of electrokinetic transport follows the order Er > Sm > La. Our findings suggest that the ionic size is a non-negligible factor affecting the electrokinetic transport of REEs in weathering crusts containing nanochannels. This work offers a constitutive model to describe the electrokinetic transport of REEs in weathering crusts, which promotes both theoretical developments and practical applications of EKM.

**Keywords:** rare earth elements; electrokinetic mining; transport model; weathering crust; ionic size



**Citation:** Wang, G.; Ling, B.; Liang, X.; Xu, J.; Kang, S.; Wei, J.; Tan, W.; Zhu, R.; Zhu, J.; He, H. Transport Model of Rare Earth Elements in Weathering Crusts during Electrokinetic Mining. *Minerals* **2024**, *14*, 360. https://doi.org/10.3390/min14040360

Academic Editor: Elizabeth Watkin

Received: 27 February 2024
Revised: 25 March 2024
Accepted: 27 March 2024
Published: 29 March 2024



## 1. Introduction

Rare earth elements (REEs) are a group of 17 strongly related elements that comprise the lanthanide group, scandium (Sc), and yttrium (Y). Due to their unique physicochemical properties, REEs play a pivotal role in emerging high technologies, such as high-capacity batteries, high-performance catalysis, functional nanomaterials, and renewable energy [1,2]. REEs can be categorized as light (LREEs) and heavy REEs (HREEs), and HREEs have been gaining increasing attention from countries worldwide due to their irreplaceability in national security applications and aerospace manufacturing [3–5]. HREEs are primarily mined from ion-adsorption deposits (IADs), which support 95% of global demand [6,7].

The primary hosting repository of IADs is the weathering crust, in which REEs exist in a hydrated cationic state and are adsorbed by clay minerals, e.g., kaolinite and halloysite [8–10]. The adsorbed REEs can be recovered by leaching, and ammonium salts

are the most commonly applied leaching agents. So far, pond leaching, heap leaching, and in situ leaching have been the most common techniques for IAD mining [11,12]. However, governmental restrictions tend to be imposed on these techniques because of several drawbacks, including grievous environmental damage, low recovery efficiency, and long leaching time [7,13–15].

Various methods have been proposed to sustainably recover REEs from weathering crusts, for example, replacing ammonium salt with magnesium salt, microorganisms, and microbial metabolisms [16–20]. A new REE mining technique, electrokinetic mining (EKM), was developed in our previous study [21–23]. By utilizing an external electric field to facilitate REE migration, the EKM technique can boost the effectiveness of REE retrieval and decrease the use of harmful chemicals. Despite the success of EKM in REE mining and many other practical applications, including metal recovery [24–26], drug delivery [27], soil remediation [28–30], and slurry dewatering [31–34], there is, as yet, no accurate model of electrokinetic transport. The existing conventional model fails to predict the transport diversity of LREEs and HREEs as observed in experiments (Figure S1).

Electrokinetic transport is a synergy among electromigration, electroosmosis, and electrophoresis [35–37]. Additionally, flow and solute-transport processes in actual weathering crust are coupled with electrolysis and geochemical reactions, which further increases the complexity of modeling [29,30]. Acar and Alshawabkeh established constitutive relations to quantify the electrokinetic flux of the aforementioned processes [38–40]. Similar models have been developed for various applications, and their results are promising [41–43]. Currently, the most common and widely used transport model is the convection–diffusion equation, which can well describe the effects of diffusion, convection, and geochemical reactions on the transport of ions [44]. Further studies of the microscopic pore structure and the flow path of solution revealed complex pore structures and blind areas in weathering crusts that influence the transport path of ions and are inclined to form a dominant flow. The transport of ions in the non-flowing and flowing zones in porous media was identified by the two-region model (TRM) [45]. Moreover, to couple the adsorption kinetics and adsorption isotherms, the one-site sorption model (OSM) and two-site sorption model (TSM) were proposed to distinguish transient and equilibrium adsorption reactions. In the OSM, the adsorption of ions in the weathering crust soil was a relatively slow process and the adsorption behavior followed the adsorption kinetic equation [46]. However, in the TSM, the adsorption reaction was divided into transient adsorption and equilibrium adsorption, and the adsorption behavior followed the multiply effect in adsorption kinetics and isotherms [47]. Meanwhile, to consider the scale of the experiment and hydrological conditions of the weathering crust soil, modular 3-dimensional transport models were also conceived [48].

However, their prediction accuracy drops when they are applied to studying REE transport in weathering crusts. The challenges are twofold: on the one hand, weathering crusts are typically low-permeability porous media (LPPM) containing nanoscale pores and channels (Figure 1), which imposes strong nanoscale effects that lead to the failure of traditional models [49–51]; on the other hand, LREEs and HREEs exhibit vast differences in transport and adsorption/desorption characteristics, and these are rarely considered in the existing models because REEs are considered to have similar physicochemical properties in most cases. Although the ionic valence and surface charge (i.e., zeta potential) have been studied in previous modeling efforts [38,39,52], the influence of the ionic size on the electrokinetic transport has not yet been addressed, especially in LPPM. Thus, a suitable weathering-crust transport model is required to distinguish the behaviors of different REEs in response to microscale features.

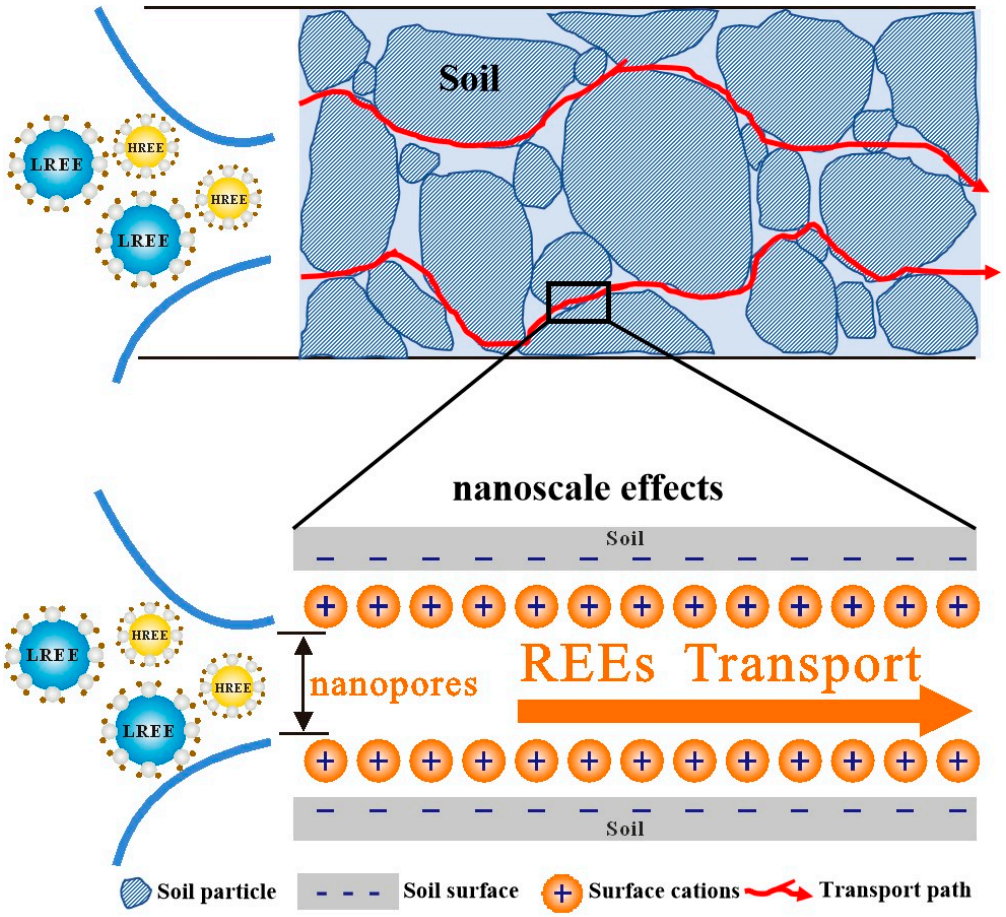


**Figure 1.** Schematics of electrokinetic transport of REEs in weathering crust containing nanoscale channels.

In this study, we developed a new transport model that accounts for the lanthanide contraction effect, a characteristic that is exclusive to REEs. This phenomenon causes the atomic and ionic radii to decrease from La to Lu, allowing for a more accurate portrayal of the electrokinetic transport of REEs and their interactions with nanoscale pores in weathering crusts. The predictions made by the newly proposed model are in good agreement with the experimental results. Intriguingly, we revealed that the electrokinetic transport velocities of HREEs and LREEs were the opposite of what might be expected when considering the influence of the ionic size, highlighting the importance of the ionic size to the electrokinetic transport of REEs in weathering crusts. This work provides a fundamental model for describing the electrokinetic transport of REEs in weathering crusts and will promote the development of both the theoretical bases and practical applications of EKM.

## 2. Materials and Methods

### *2.1. Materials*

The weathering crusts were collected from the topsoil of a weathering profile in Maofeng Mountain (113.46° E, 23.30° N), Guangzhou, China. Samples were naturally dried at 298.15 K and crushed to pass through a 0.9 mm mesh for the removal of roots and sand before being used. The REE stock solutions were obtained by dissolving their corresponding nitrates with deionized water. Lanthanum (III) nitrate hexahydrate [$La(NO_3)_3 \cdot 6H_2O$, 99.99%], samarium (III) nitrate hexahydrate [$Sm(NO_3)_3 \cdot 6H_2O$, 99.99%], erbium (III) nitrate hexahydrate [$Er(NO_3)_3 \cdot 6H_2O$, 99.99%], yttrium (III) nitrate hexahydrate [$Y(NO_3)_3 \cdot 6H_2O$, 99.99%], and ammonium sulfate [$(NH_4)_2SO_4$, 99.99%] were purchased from Aladdin Industrial Co., Shanghai, China.

### 2.2. Electrokinetic Transport Experiments with REEs in Weathering Crust

The electrokinetic experiments were carried out using a homemade setup (Figure 2) containing a cuboid soil chamber [(50 × 4 × 4) $cm^3$], a receiving tank, and a power supply equipped with a DC stabilizer (5A32V, Lodestar, Shenzhen, China). Initially, 1000 g of the weathering crust was put into the soil chamber and compressed to a height of 4 cm, achieving a bulk density of 1.20 $g/cm^3$. Then, 200 mL of deionized water was pumped into the soil chamber to prewet the weathering crust, achieving a water content of ~20%. Two graphene electrodes were placed on each side of the soil chamber to act as the anode and the cathode. The electrodes were drilled, producing numerous 0.5 mm holes to allow the REE solution and water to flow through them. The electrodes and the soil were separated by geotextile to prevent soil particles from being washed out. After this, a series of LREE (La and Sm) and HREE (Er) solutions were added to the anodic chamber, the height of which was kept at 4.5 cm (slightly higher than the height of the soil sample, i.e., 4 cm) by using a constant-pressure bottle. Finally, the system was subjected to an applied electric field with a voltage gradient of 100 $V \cdot m^{-1}$. The REE concentrations at different positions (P1, P2, P3, and P4, with distances from the anode of 1.5, 16.5, 31.5, and 46.5 cm, respectively) in the weathering crust were detected at various time intervals and analyzed by inductively coupled plasma optical emission spectrometry (ICP-OES).

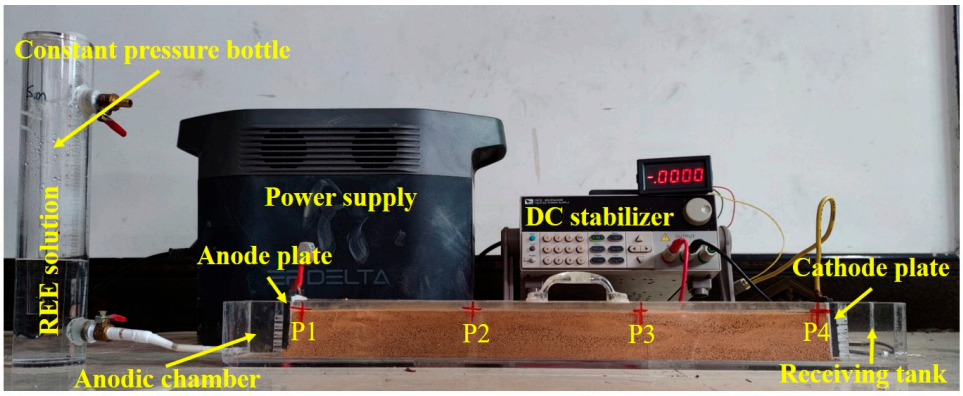


**Figure 2.** Photograph of the electrokinetic transport setup.

### 2.3. Adsorption Experiments

The adsorption performance of the weathering crust for LREEs and HREEs was evaluated based on adsorption isotherms, which were performed at a pH of 5.5 (the natural pH of topsoil) and an ambient temperature of 25 °C. In a typical batch model, 5 g of each sample was dispersed into 50 mL of working solutions containing a series of REE (La, Sm, and Er) concentrations (50–500 mg/L). After complete adsorption for 6 h, 1 mL of the supernatant was separated from the system using a 0.22 μm membrane filter. The equilibrium concentrations before and after adsorption were determined by ICP-OES analysis. All adsorption experiments were repeated in triplicate, and the mean values and standard deviations of these values are presented. The adsorption amount at equilibrium ($q_e$, mg/kg) was calculated according to:

$$q_e = \frac{(c_0 - c_e) \times V}{m}, \quad (1)$$

where $c_0$ and $c_e$ (mg/L) are the REE concentrations in solution before and after adsorption, respectively, $V$ (L) is the REE solution volume, and $m$ (kg) is the soil weight.

The adsorption data were fitted with the Langmuir isotherm model to calculate the saturated maximum adsorption capacity. The Langmuir isotherm model assumes that the adsorption proceeds by the formation of a monolayer, meaning that no further adsorption occurs once the adsorbate has been adsorbed at a particular site. The Langmuir isotherm

model was applied to calculate the maximum adsorption capacities of the weathering crust for three REEs (La, Sm, and Er). The relationship is expressed as:

$$\frac{c_e}{q_e} = \frac{1}{q_m}c_e + \frac{1}{q_m K_L}, \quad (2)$$

where $q_m$ represents the maximum adsorption capacity of the adsorbent (mg/g) and $K_L$ is the Langmuir constant (L/mg). The experimental values of $q_m$ and $K_L$ were calculated from the slope and intercept of the linear plot of $c_e/q_e$ against $c_e$.

### *2.4. Column Leaching Experiments*

Column leaching experiments were conducted using an acrylic column (inner diameter 6 cm, column length 15 cm), into which 350 g of the weathering crust was placed and compacted to a height of 10.5 cm (particle density 1.2 g/cm$^3$). Deionized water was initially pumped upward through the column using a peristaltic pump to flush the weathering crust sample until a steady-state flow was established. Approximately 4.5 L of deionized water was consumed before initiating the transport experiments. Then, 10 L of each REE solution (La, Sm, and Er; 100 mg/L) was introduced downward into the packed column with a hydraulic head of 3 cm. The REEs were then transported through the column with a flow velocity of around 3 mL/min. The leachates were collected at various time intervals and measured using ICP-OES to determine the REE concentrations. Breakthrough curves were then obtained by plotting dimensionless effluent concentrations ($c/c_0$, where $c$ and $c_0$ are the influent and initial concentrations, respectively) of the REEs as a function of time.

### *2.5. Analytical Methods*

X-ray diffraction (XRD) measurements were taken on a Bruker D8 Advance diffractometer (copper source, 40 kV and 40 mA); patterns were collected over an angular range of 3–80° 2θ with a step size of 0.01° and a scan speed of 5°/min. Scanning electron microscopy (SEM) images were acquired by using a Hitachi SU8010 microscope (Hitachi, Tokyo, Japan), and the samples were coated with gold to increase their electrical conductivity. The REE concentrations were measured by ICP-OES using an Agilent 730 spectrometer (Agilent, California, USA). The solid samples were first dried in an oven at 378.15 K and then ground into powder to pass through a 0.74 μm mesh. A total of 1 g of each pretreated sample was added into a 15 mL centrifuge tube containing 10 mL of 0.2 mol/L $(NH_4)_2SO_4$. The mixture was allowed sufficient reaction time in a shaker for 12 h or overnight. After this, the mixture was centrifuged, and the supernatant was filtered through a 0.22-μm filter membrane before being acidified with ultrapure concentrated nitric acid (1% $v/v$). The bulk density ($\rho_b$) of the weathering crust was measured by the cutting-ring sampling method. Briefly, after weighing, soaking, and drying, the soil bulk density was calculated according to:

$$\rho_b = \frac{m_1 - m_h}{100 + 100 \times D}, \quad (3)$$

where $m_1$ (g) is the initial weight of the soil sample including the cutting ring, $m_h$ (g) is the weight of the cutting ring, and $D$ (cm$^3$) is the volume of the cutting ring, respectively. The total porosity ($\phi$) of the weathering crust was calculated according to the measured bulk density ($\rho_b$) using:

$$\varnothing = \left(1 - \frac{\rho_b}{\rho}\right) \times 100\%, \quad (4)$$

where $\rho$ is the specific gravity of the soil (g/cm$^3$). The real tortuosity ($\tau$) can be obtained by averaging over all possible configurations for flow path in porous media. For simplicity, this

work roughly considers two idealized configurations, i.e., some particles are overlapped and the others are not. The averaged tortuosity is thus expressed as Equation (5):

$$\tau = \frac{1}{2}\left[1 + \frac{1}{2}\sqrt{1-\varnothing} + \sqrt{1-\varnothing}\,\frac{\sqrt{\left(\frac{1}{\sqrt{1-\varnothing}} - 1\right)^2 + \frac{1}{4}}}{1-\sqrt{1-\varnothing}}\right], \tag{5}$$

As such, the $\tau$ is a function of porosity only. The diffusion coefficients ($D_i$) in infinitely dilute solution and ionic radii ($r$) of REEs are discussed the literature [39,53].

## 3. Results and Discussion

### *3.1. Construction of the Electrokinetic Transport Model*

To quantify the electrokinetic transport of species under an electric field, we adopt the framework proposed by Alshawabkeh and colleagues [40]. Considering a solution at infinite dilution, the equation for ionic electromigration is:

$$v_{\text{solution}} = \mu_i E, \tag{6}$$

where $v_{\text{solution}}$ ($\text{m}\cdot\text{s}^{-1}$) is the electromigration velocity of an ion, $\mu_i$ ($\text{m}^2\cdot\text{V}^{-1}\cdot\text{s}^{-1}$) is the ionic mobility of an ion, and $E$ ($\text{V}\cdot\text{m}^{-1}$) is the electric potential (i.e., the applied voltage gradient between the anode and the cathode). The ionic electromigration in LPPM is expressed as:

$$v_{\text{LPPM}} = {\mu_i}^* E, \tag{7}$$

where ${\mu_i}^*$ ($\text{m}^2\cdot\text{V}^{-1}\cdot\text{s}^{-1}$) represents the ionic mobility of an ion in LPPM.

In the conventional models, ${\mu_i}^*$ has been modified to include the effective properties—porosity ($\phi$) and tortuosity ($\tau$)—of LPPM:

$${\mu_i}^* = \phi\tau\mu_i \tag{8}$$

where $\phi$ and $\tau$ are nondimensional constants that can be determined by experiments. Based on the Nernst–Townsend–Einstein relation, $\mu_i$ can be estimated using the molecular diffusion coefficient $D_i$ and expressed as:

$$\mu_i = D_i\frac{ZF}{RT} \tag{9}$$

where $D_i$ ($\text{m}^2\cdot\text{s}^{-1}$) is the diffusion coefficient of an ion in solution at infinite dilution, $Z$ is the ionic valence, $F$ ($\text{C}\cdot\text{mol}^{-1}$) is Faraday's constant, $R$ is the universal gas constant ($8.314\ \text{J}\cdot\text{K}^{-1}\cdot\text{mol}^{-1}$), and $T$ (K) is the absolute temperature. The ionic mobility (${\mu_i}^*$) and electromigration velocity ($v_{\text{LPPM}}$) of an ion in LPPM are:

$${\mu_i}^* = \phi\tau D_i\frac{ZF}{RT} \tag{10}$$

$$v_{\text{LPPM}} = \phi\tau D_i\frac{ZF}{RT}E = \frac{\phi\tau ZFE}{RT}D_i \tag{11}$$

As mentioned above, for electrokinetic transport of REEs in weathering crust containing large numbers of nanochannels, the effect of the ionic size cannot be neglected. Mobile ions with larger effective radii are expected to experience greater resistance than those with smaller effective radii, and this will likely result in lower ionic mobilities and electromigration velocities. To include the effect of the ionic size on the electrokinetic transport of REEs in weathering crust, ${\mu_i}^*$ is further modified by introducing the effective ionic radius factor ($\alpha_r$):

$${\mu_i}^{**} = \frac{\phi\tau\mu_i}{\alpha_r}, \tag{12}$$

where $\alpha_r$ is a nondimensional constant to represent the effect of the ionic size.

The relation for describing the electromigration velocities ($v^*_{WC}$) of REEs in weathering crusts is modified accordingly:

$$v^*_{WC} = \phi\tau\frac{D_i ZF}{\alpha_r RT}E = \frac{\phi\tau ZFE}{\alpha_r RT}D_i \quad (13)$$

Previous studies have suggested that the magnitude of mass transport by electromigration is often at least an order of magnitude higher than that induced by electroosmosis [38,39], and mass transport by electrophoresis is negligible in most cases [29]. Thus, the impacts of ionic size on electroosmosis and electrophoresis are not discussed here.

### *3.2. Precidition Results of REE Transport by Electrokinetic Transport Models*

The electrokinetic transport of REEs in weathering crust can be predicted based on the above relations. As shown in Table 1, in an infinitely dilute solution, the diffusion coefficient $D_i$ decreases from La ($0.619 \times 10^{-9}$ $m^2/s$) to Yb ($0.582 \times 10^{-9}$ $m^2/s$), to Sc ($0.574 \times 10^{-9}$ $m^2/s$) and Y ($0.550 \times 10^{-9}$ $m^2/s$). According to the conventional model [Equation (10)], the ionic mobility in weathering crust also decreases from La ($16.568 \times 10^{-9}$ $m^2/Vs$) to Yb ($15.578 \times 10^{-9}$ $m^2/Vs$), to Sc ($15.364 \times 10^{-9}$ $m^2/Vs$) and Y ($14.722 \times 10^{-9}$ $m^2/Vs$) [Figure 3a]. The same trend holds for the electromigration velocities (assuming 100 $V \cdot m^{-1}$ of applied voltage gradient) of REEs in weathering crust based on Equation (11) [Figure S2a]. The electrokinetic transport of REEs in weathering crust is predicted to show similar behavior as that in bulk solutions. This is because all REEs are subjected to the same conditions, including electric potential ($E$), temperature ($T$), soil porosity ($\phi$), and tortuosity ($\tau$), and both the electromigration velocities ($v_{LPPM}$) and effective ionic mobilities ($\mu_i^*$) of REEs in weathering crusts depend only on their diffusion coefficients $D_i$ according to the conventional models [Equations (10) and (11)]. Generally, according to the conventional models, the electrokinetic transport of LREEs (La–Eu) in weathering crusts should be faster than that of HREEs (Gd–Lu, Sc, and Y). However, the conventional models neglect the impact of the ionic size on the electrokinetic transport of REEs in weathering crusts.

**Table 1.** Diffusion coefficients ($D_i$) in infinitely dilute solution and effective ionic mobilities ($\mu_i^*$) of REEs in weathering crust as predicted by the conventional and newly proposed (modified) models.

| REEs | $D_i \times 10^9$ $m^2/s$ | Ionic radius Å | Conventional $\mu_i^* \times 10^9$ $m^2/Vs$ | Modified $\mu_i^* \times 10^9$ $m^2/Vs$ |
|---|---|---|---|---|
| $La^{3+}$ | 0.619 | 1.18 | 16.568 | 14.041 |
| $Ce^{3+}$ | 0.620 | 1.14 | 16.595 | 14.557 |
| $Pr^{3+}$ | 0.617 | 1.14 | 16.515 | 14.487 |
| $Nd^{3+}$ | 0.616 | 1.12 | 16.488 | 14.722 |
| $Pm^{3+}$ | ND | 1.10 | ND | ND |
| $Sm^{3+}$ | 0.608 | 1.09 | 16.274 | 14.930 |
| $Eu^{3+}$ | 0.602 | 1.07 | 16.113 | 15.059 |
| $Gd^{3+}$ | 0.597 | 1.06 | 15.980 | 15.075 |
| $Tb^{3+}$ | ND | 1.04 | ND | ND |
| $Dy^{3+}$ | 0.582 | 1.03 | 15.578 | 15.124 |
| $Ho^{3+}$ | 0.589 | 1.02 | 15.765 | 15.456 |
| $Er^{3+}$ | 0.585 | 1.00 | 15.658 | 15.658 |
| $Tm^{3+}$ | 0.581 | 0.99 | 15.551 | 15.708 |
| $Yb^{3+}$ | 0.582 | 0.98 | 15.578 | 15.896 |
| $Lu^{3+}$ | ND | 0.97 | ND | ND |
| $Sc^{3+}$ | 0.574 | 0.87 | 15.364 | 17.660 |
| $Y^{3+}$ | 0.550 | 1.02 | 14.722 | 14.504 |

Note: ND indicates that there is no $D_i$ value recorded for this REE.

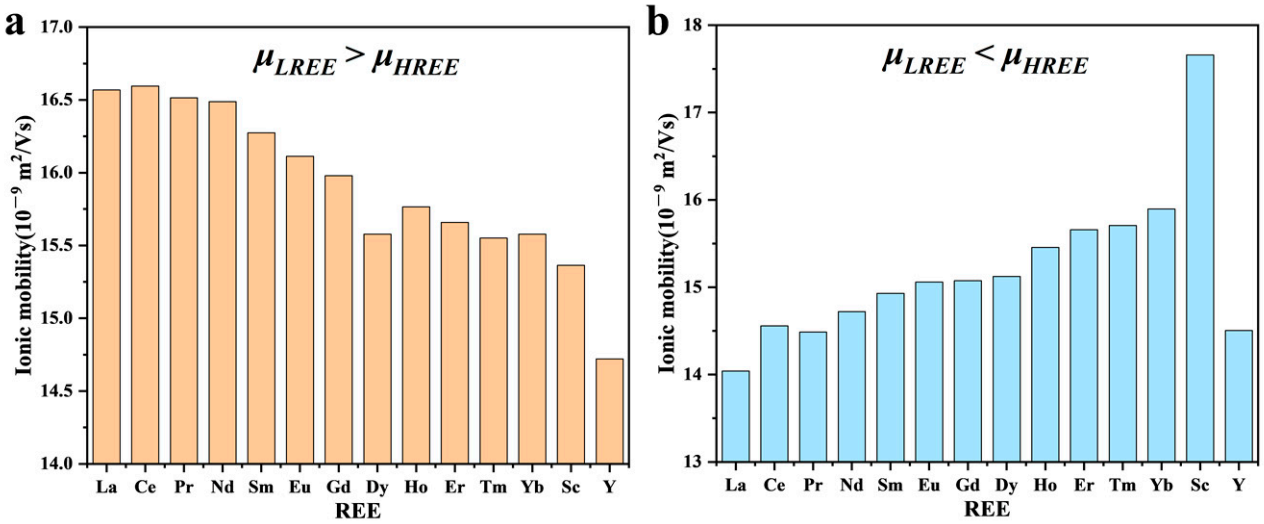


**Figure 3.** Theoretical effective ionic mobilities of REEs in weathering crust calculated based on the (**a**) conventional and (**b**) newly proposed models.

The transport properties of REEs in weathering crusts may be different from those in bulk solutions. Due to lanthanide contraction, the effective ionic radii of REEs decrease from La (1.18 Å) to Lu (0.97 Å). The effective ionic radii of Sc and Y are 0.87 and 1.02 Å, respectively. We adopted the values of effective ionic radii of REEs as nondimensional parameters $\alpha_r$ to evaluate the effects of ionic size. Based on the modified model [Equation (12)], the ionic mobilities of REEs in the weathering crust are predicted to increase from La ($14.041 \times 10^{-9}$ m$^2$/Vs) to Yb ($15.896 \times 10^{-9}$ m$^2$/Vs), and to Sc ($17.660 \times 10^{-9}$ m$^2$/Vs) [Figure 3b]. According to Equation (13), the electromigration velocities (assuming 100 V·m$^{-1}$ of applied voltage gradient) of REEs in the weathering crust are also predicted to increase from La ($1.404 \times 10^{-6}$ m/s) to Yb ($1.590 \times 10^{-6}$ m/s), and to Sc ($1.766 \times 10^{-6}$ m/s) [Figure S2b]. Interestingly, the predictions of the modified model [Equations (12) and (13)] are completely contrary to those of the conventional model [Equations (10) and (11)], i.e., HREEs transport faster than LREEs in weathering crusts. Moreover, the electrokinetic transport of REEs in weathering crusts is different from that in bulk solutions, highlighting the impact of the ionic size. There is an anomaly in the electrokinetic transport of Y because the diffusion coefficient and effective ionic radius of Y are different from those of the lanthanides (La–Lu). Sc displays the highest ionic mobility ($17.660 \times 10^{-9}$ m$^2$/Vs) and electromigration velocity ($1.766 \times 10^{-6}$ m/s), and this is probably due to it having the smallest effective ionic radius (i.e., 0.87 Å) among the REEs.

### *3.3. Experimental Validation of the Electrokinetic Transport Model*

To validate the predictions of the proposed model, electrokinetic transport experiments were carried out with REEs in an actual weathering crust. The weathering crust was collected from a granite weathering profile on Maofeng Mountain, Guangzhou, China. The porosity ($\phi$) and tortuosity factor ($\tau$) of this weathering crust were 0.3099 and 0.6774, respectively (Table 2). Its main minerals were quartz, kaolinite, and halloysite (Figure 4). The initial ion-exchangeable REE concentration in the weathering crust was 206.62 mg/kg (Table 2). The reason for choosing a natural weathering crust was that the adsorption of REEs on the clay minerals of the weathering crust would have reached equilibrium during the long-term formation of the IAD.

**Table 2.** Properties of the weathering crust sample for electrokinetic experiments. Unit: mg/kg.

| REE | La | Ce | Pr | Nd | Sm | Eu | Gd | Tb | Dy | Y | Ho | Er | Tm | Yb | Lu | ΣREE |
|---|---|---|---|---|---|---|---|---|---|---|---|---|---|---|---|---|
| Cont. | 49.64 | 45.01 | 10.84 | 54.73 | 8.74 | 1.16 | 5.25 | 0.48 | 4.17 | 20.08 | 0.79 | 2.39 | 0.10 | 2.85 | 0.40 | 206.62 |
| Porosity | 0.3099 | Tortuosity factor | | 0.6774 | Mineral composition | | | quartz | | kaolinite | | halloysite | | | | |

The experimental setup is illustrated in Figure 5a, and more details are presented in the Methods Section. Two LREEs (La and Sm) and one HREE (Er) with the same concentrations (200 ppm) were used as representative REEs and transported through the weathering crust under an electric field (100 $V \cdot m^{-1}$). The variations of REE concentrations at different positions (P1, P2, P3, and P4 from the anode to the cathode) in the weathering crust were monitored at various time intervals. Notably, the REE concentrations at P1–P3 were in the order Er > Sm > La at all electrokinetic treatment times [Figure 5b–d], suggesting that the electrokinetic transport velocity of the HREE (Er) is faster than those of the LREEs (La and Sm); this is consistent with the predictions of the newly proposed model [Figure 3b and Table 1]. The REE concentrations at P4 are not presented because La and Sm were not detected within the experimental period (0–144 h). To estimate the electrokinetic transport velocities of the REEs, we analyzed the migration distances of their leading edges over time. Experimentally, we determined these distances by monitoring the REE concentrations at various locations within the weathering crust. If the concentration exceeded zero, we inferred that the REE had surpassed the measuring point [42].

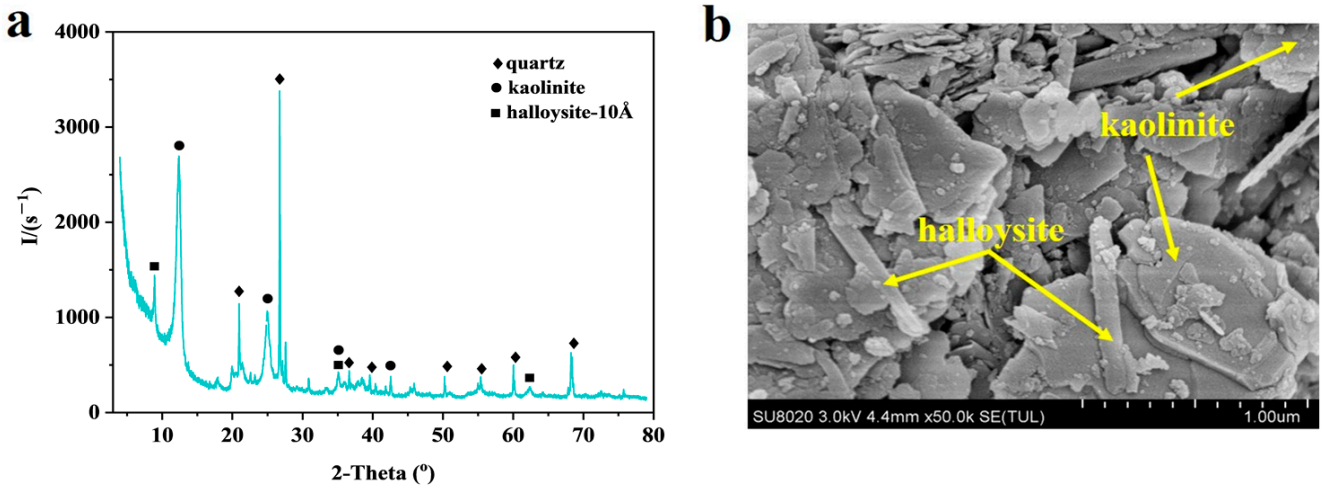


**Figure 4.** (**a**) XRD pattern and (**b**) SEM image of the weathering crust sample (scale bar = 1 μm).

The transport distances of all three REEs (La, Sm, and Er) displayed a nearly linear progression with electrokinetic treatment time [Figure 5e], suggesting a constant REE migration velocity. The mean transport velocities for La, Sm, and Er were calculated to be 0.2188, 0.3129, and 0.6300 cm/h, respectively, clearly demonstrating that the HREE transported faster than the LREEs. These experimental results confirm that the trend in the REE electrokinetic transport velocities in weathering crust is opposite of that in bulk solutions, and the newly proposed model can distinguish the transport diversity of LREEs and HREEs. Notably, the inversion of the expected electrokinetic transport velocities of LREEs and HREEs highlights the impact of the ionic size.

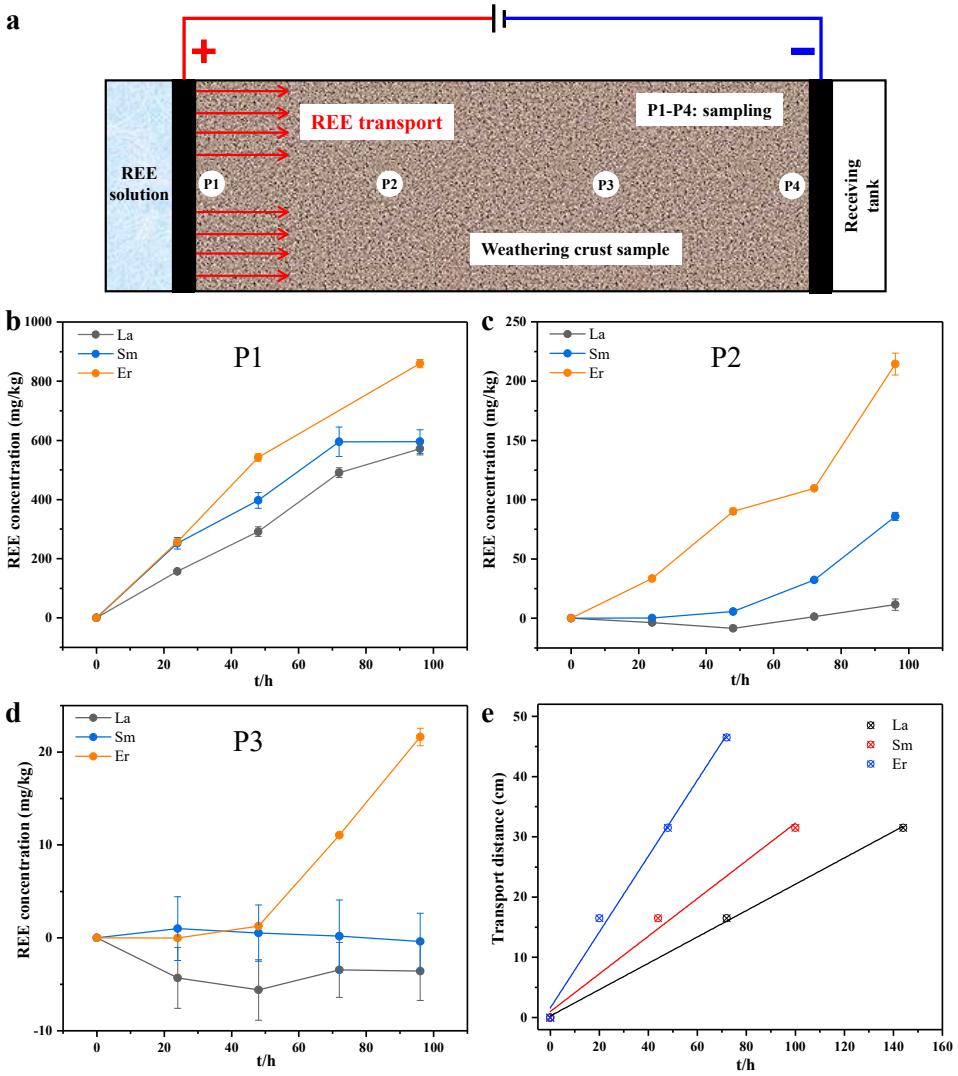


**Figure 5.** Experimental results of electrokinetic transport of La, Sm, and Er in weathering crust. (**a**) Setup of the electrokinetic experiments. (**b**–**d**) Variations of REE concentrations in P1, P2, and P3 as a function of time. (**e**) Electrokinetic transport distances of La, Sm, and Er in weathering crust as a function of time.

### *3.4. Influence of Adsorption*

The inverted electrokinetic transport velocities may raise concerns about varying adsorption rates in the weathering crust for LREEs and HREEs. It is possible that if the weathering crust absorbed more LREEs, the HREEs would move at a faster rate than the LREEs. To address this potential influence on the electrokinetic transport of REEs, we conducted batch adsorption experiments for La, Sm, and Er using the weathering crust (see methods for experimental details). The resulting adsorption isotherms are displayed in Figure 6a. Previous studies have suggested that the adsorption of REEs in weathering crusts fits the Langmuir model best when compared with other isothermal models [54]. Based on the Langmuir model, the maximum adsorption capacities of the weathering crust for La, Sm, and Er were calculated to be 1.66, 2.12, and 2.42 mg/kg, respectively (Table 3), suggesting that more HREEs than LREEs will be adsorbed by the weathering crust. This result supports the idea that LREEs transport faster than HREEs in weathering crusts; it is, however, inconsistent with the experimental results.

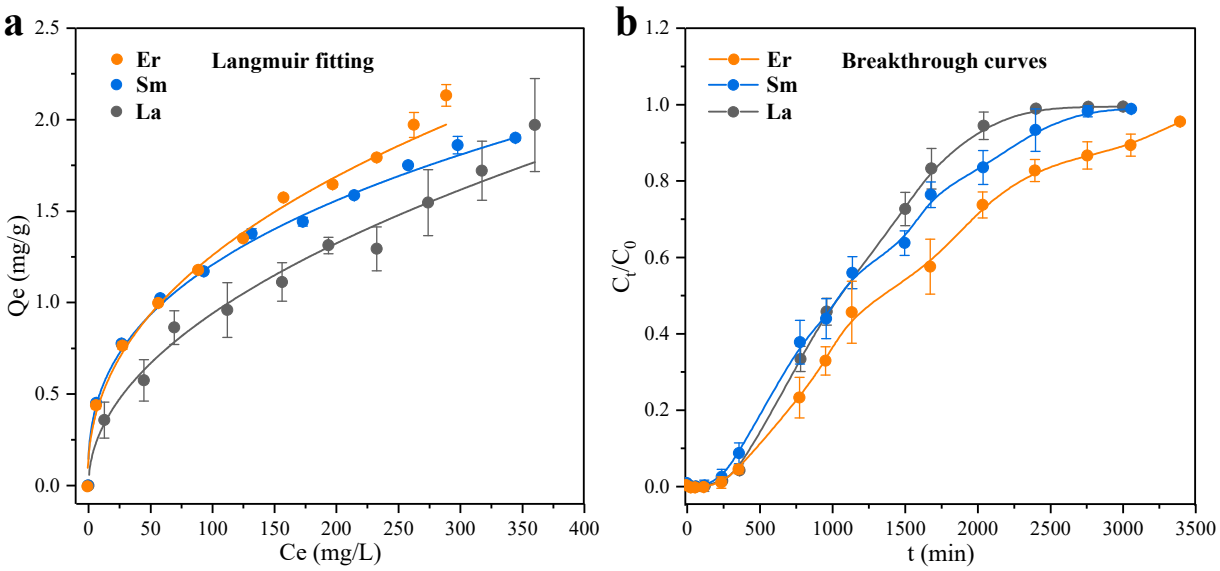


**Figure 6.** Adsorption properties of the weathering crust for REEs. (**a**) Adsorption isotherms for La, Sm, and Er with Langmuir-model fitting. (**b**) Breakthrough curves of La, Sm, and Er.

**Table 3.** Parameters of the Langmuir isotherm model for REE adsorption on the weathering crust.

| REE | Langmuir Model | | |
|---|---|---|---|
| | Qmax (mg/g) | KL (L/mg) | $R^2$ |
| La | 1.6614 | 0.0148 | 0.9681 |
| Sm | 2.1236 | 0.0174 | 0.9751 |
| Er | 2.4160 | 0.0140 | 0.9476 |

It is noted that the batch adsorption experiments were carried out in bulk solutions (5 g of the weathering crust sample was dispersed in centrifuge tubes containing 50 mL solutions with a series of concentrations of REEs), which involves a different adsorption process from that occurring when the weathering crust is in a compacted state. As such, breakthrough experiments (i.e., column leaching with REE solutions under natural gravity) were performed to investigate the adsorption of REEs on weathering crust that was confined in a column (see methods for experimental details). The leachates were collected at certain time intervals and analyzed to determine the REE concentrations.

The breakthrough curves [Figure 6b] show that the collected REE concentrations in the leachates were in the order La > Sm > Er at any given leaching time, and the breakthrough times were 2400, 2800, and 3200 min for La, Sm, and Er, respectively. These results suggest that similar to the trend observed with bulk solutions, the adsorption of HREEs in the weathering crust is higher than that of LREEs even though the weathering crust is in a compact state. Consequently, adsorption by the weathering crust is excluded from the possible reasons for the reversal of the order of LREE and HREE electrokinetic transport velocities.

### *3.5. Mechanism for the Electrokinetic Transport Diversity between LREEs and HREEs*

The mechanism that results in the mobility diversity of LREEs and HREEs in an electric field is discussed below. Theoretically, the migration of REEs in an electric field and a low-permeability porous media can be regarded as driven by a combination of forces of electric field ($F_{elect}$) and viscous resistance ($F_{resist}$) where $F_{elect}$ and $F_{resist}$ can be calculated by Equation (14) and Equation (15), respectively. As driven by the combined forces, REEs will initially transport at an accelerated speed before reaching a constant velocity when

$F_{elect} = F_{resist}$, which is the equilibrium migration rate ($V_E$, m/s) of REEs. As such, the $V_E$ of REEs can be calculated according to Equation (16).

$$F_{elect} = EQ = Enq|Z| \tag{14}$$

$$F_{resist} = 6\pi\eta r V_E \tag{15}$$

$$V_E = \frac{Eq|Z|}{6\pi\eta r} \tag{16}$$

where $E$ (V/m) is the electric field intensity, $Q$ (C) is the charge quantity, n is the number of REEs, $q$ ($\approx 1.60 \times 10^{-19}$ C) is the quantity of elementary charge, $Z$ is the valence that is +3 for all REEs, $\eta$ (Pa·s) is the dynamic viscosity, and $r$ (nm) is the effective ion radius.

According to Equation (16), the migration rate of REEs is positively correlated with the electric field intensity and the valence of REEs, but it is negatively correlated with the dynamic viscosity and effective ion radius of REEs. As LREEs and HREEs are subjected to the same electric field and have the same valence, the migration rates are negatively related to their ion radii and dynamic viscosity. The dynamic viscosity of each REE in the weathering crust soil is related to the soil parameters (e.g., porosity $\phi$ and tortuosity $\tau$) and diffusion coefficients $D_{\mathrm{i}}$ in an infinitely dilute solution. Consequently, the equilibrium migration rate ($V_E$,) of each REE is jointly determined by the ion radius and diffusion coefficient of an REE, in line with the proposed transport model. Considering the lanthanide contraction, HREE generally transports faster than LREE.

Note that REEs migrate in the form of hydrated, inorganic, and/or organic complexes in weathering crusts and the effective ion radius is affected by various factors. For example, speciation studies [55,56] of REEs in aqueous fluid at ambient temperatures and neutral pH suggest that the smaller HREEs (Gd-Lu) favor an 8-fold hydration sphere (the coordination number (CN) = 8), whereas the larger LREEs (La-Eu) and Y favor 9-fold coordination (CN = 9). Therefore, the radius of the hydrated or complex REE should be considered when evaluating the mobility of REEs in an electric field.

## 4. Conclusions

To summarize, our findings demonstrate that the electrokinetic transport of REEs in the nanochannels of weathering crusts is influenced by their ionic size, leading to a reversal of the expected order of electrokinetic transport velocities for HREEs and LREEs. We have developed a new transport model that considers the lanthanide contraction effect, providing a more precise description of REE electrokinetic transport in weathering crusts and distinguishing between the mobility of different REEs. Additionally, we excluded the influence of weathering crust adsorption on different REEs through batch adsorption and breakthrough experiments. Our research offers a constitutive model to depict the electrokinetic transport of REEs in weathering crusts, contributing to both theoretical advancements and practical uses of EKM for REE recovery. For example, we can design mining parameters and set collection sites for recovering REE based on the precise prediction of REE transport. By comprehending REE fractionation during electrokinetic transport, we can potentially separate and pre-enrich LREEs and HREEs. Additionally, this enhances our understanding of transport physics in nanoscale channels, providing opportunities to enhance the utilization of electrokinetic technology. Understanding element transport as well as the controlling factors in porous media not only has important implications for interpreting some geochemical behaviors, such as element cycling, enrichment, and fractionation, but also provides fresh insights for manufacturing as it can be applied to diverse fields, such as chemical separation, drug delivery, soil remediation, and nanodevice fabrication. Note that, the newly proposed model focuses on REE transport in weathering crusts. Further studies should be carried out in different media to evaluate the universality of the proposed model.

**Supplementary Materials:** The following supporting information can be downloaded at: https://www.mdpi.com/article/10.3390/min14040360/s1, Figure S1: (**a**) Variation of LREE/HREE ratio in the collected leachate with increasing EKM treatment time. (**b**) LREE/HREE ratio in weathering crust after the EKM treatment; Figure S2: Electromigration velocities of REEs in weathering crust calculated based on the (**a**) conventional and (**b**) newly proposed models.

**Author Contributions:** Conceptualization, H.H. and J.Z.; methodology, G.W. and W.T.; software, G.W.; validation, G.W., B.L. and X.L.; formal analysis, J.X.; investigation, G.W., J.X. and S.K.; resources, J.W.; data curation, G.W. and R.Z.; writing—original draft preparation, G.W.; writing—review and editing, G.W., B.L., X.L., H.H. and J.Z.; visualization, G.W. and J.X.; supervision, H.H. and J.Z.; project administration, H.H. and J.Z.; funding acquisition, H.H., J.Z., G.W. and B.L. All authors have read and agreed to the published version of the manuscript.

**Funding:** This work was supported by National Natural Science Foundation of China (41825003, J.Z.; 42102037, G.W.; 42272158, B.L.); the Strategic Priority Research Program of the Chinese Academy of Sciences (XDA0430205, H.H.); Guangdong Major Project of Basic and Applied Basic Research (2019B030302013, H.H.); Guangdong Basic and Applied Basic Research Foundation (2023A1515012927, G.W.); and Science and Technology Planning of Guangdong Province, China (2023B1212060048, J.Z.).

**Data Availability Statement:** The data that support the findings of this study are available from the corresponding author upon reasonable request.

**Acknowledgments:** This is contribution No. IS-3487 from GIGCAS and we would like to thank Yongjin Xu and Linigyu Ran in our group for their support in conducting EKM experiments and constructive suggestions.

**Conflicts of Interest:** Authors declare that they have no competing interests.

## References

1. Dushyantha, N.; Batapola, N.; Ilankoon, I.M.S.K.; Rohitha, S.; Premasiri, R.; Abeysinghe, B.; Ratnayake, N.; Dissanayake, K. The story of rare earth elements (REEs): Occurrences, global distribution, genesis, geology, mineralogy and global production. *Ore Geol. Rev.* **2020**, *122*, 103521. [CrossRef]
2. Acharya, S.; Dey, D.; Maitra, T.; Soni, A.; Taraphder, A. Rare earth doping and effective band-convergence in SnTe for improved thermoelectric performance. *Appl. Phys. Lett.* **2018**, *113*, 193904. [CrossRef]
3. Xu, C.; Kynicky, J.; Smith, M.P.; Kopriva, A.; Brtnicky, M.; Urubek, T.; Yang, Y.; Zhao, Z.; He, C.; Song, W. Origin of heavy rare earth mineralization in South China. *Nat. Commun.* **2017**, *8*, 14598. [CrossRef] [PubMed]
4. Li, M.Y.H.; Zhou, M.-F.; Williams-Jones, A.E. The genesis of regolith-hosted heavy rare earth element deposits: Insights from the world-class Zudong deposit in Jiangxi province, South China. *Econ. Geol.* **2019**, *114*, 541–568. [CrossRef]
5. Liu, S.-L.; Fan, H.-R.; Liu, X.; Meng, J.; Butcher, A.R.; Yann, L.; Yang, K.-F.; Li, X.-C. Global rare earth elements projects: New developments and supply chains. *Ore Geol. Rev.* **2023**, *157*, 105428. [CrossRef]
6. Li, M.Y.H.; Zhou, M.-F.; Williams-Jones, A.E. Controls on the dynamics of rare earth elements during subtropical hillslope processes and formation of regolith-hosted deposits. *Econ. Geol.* **2020**, *115*, 1097–1118. [CrossRef]
7. Yang, X.J.; Lin, A.; Li, X.-L.; Wu, Y.; Zhou, W.; Chen, Z. China's ion-adsorption rare earth resources, mining consequences and preservation. *Environ. Dev.* **2013**, *8*, 131–136. [CrossRef]
8. Bao, Z.; Zhao, Z. Geochemistry of mineralization with exchangeable REY in the weathering crusts of granitic rocks in South China. *Ore Geol. Rev.* **2008**, *33*, 519–535. [CrossRef]
9. Sanematsu, K.; Watanabe, Y. Characteristics and genesis of ion adsorption-type rare earth element deposits. *Rev. Econ. Geol* **2016**, *18*, 55–79.
10. Li, Y.H.M.; Zhao, W.W.; Zhou, M.F. Nature of parent rocks, mineralization styles and ore genesis of regolith-hosted REE deposits in South China: An integrated genetic model. *J. Asian Earth Sci.* **2017**, *148*, 65–95. [CrossRef]
11. Nie, W.; Zhang, R.; He, Z.; Zhou, J.; Wu, M.; Xu, Z.; Chi, R.; Yang, H. Research progress on leaching technology and theory of weathered crust elution-deposited rare earth ore. *Hydrometallurgy* **2020**, *193*, 105295. [CrossRef]
12. He, Z.; Zhang, R.; Nie, W.; Zhang, Z.; Chi, R.; Xu, Z.; Wu, M.; Qu, J. Leaching process and mechanism of weathered crust elution-deposited rare earth ore. *Min. Metall. Explor.* **2019**, *36*, 1021–1031. [CrossRef]
13. Lee, J.C.K.; Wen, Z. Rare earths from mines to metals: Comparing environmental impacts from China's main production pathways. *J. Ind. Ecol.* **2017**, *21*, 1277–1290. [CrossRef]
14. Li, W.; Zuo, Y.; Wang, L.; Wan, X.; Yang, J.; Liang, T.; Song, H.; Weihrauch, C.; Rinklebe, J. Abundance, spatial variation, and sources of rare earth elements in soils around ion-adsorbed rare earth mining areas. *Environ. Pollut.* **2022**, *313*, 120099. [CrossRef] [PubMed]
15. Bai, J.; Xu, X.; Duan, Y.; Zhang, G.; Wang, Z.; Wang, L.; Zheng, C. Evaluation of resource and environmental carrying capacity in rare earth mining areas in China. *Sci. Rep.* **2022**, *12*, 6105. [CrossRef] [PubMed]

16. Guo, Q.; Li, Z.; Pan, J.; Li, B.; Zhao, L.; Liu, D.; Zheng, X.; Wang, C. Leaching Mechanism of Aluminum during Column Leaching of Ion-Adsorption Rare Earth Ore Using Magnesium Sulfate. *Minerals* **2023**, *13*, 401. [CrossRef]
17. Gao, Z.; Rao, Y.; Zhang, X.; Xu, W.; Yang, Z.; Xiang, R. Calculation of Shear Layer Thickness of Ionic Rare Earth Particles in Mixture Electrolytes during In-Situ Leaching Process. *Minerals* **2023**, *13*, 733. [CrossRef]
18. Chen, J.; Qiu, J.; Huang, L.; Chen, X.; Yang, Y.; Xiao, Y. Coordination–reduction leaching process of ion-adsorption type rare earth ore with ascorbic acid. *J. Rare Earths* **2023**, *41*, 1225–1233. [CrossRef]
19. Zhou, H.; Yu, X.; Wang, J.; Qiu, G.; Zhao, H.; Shen, L. Utilization of Aspergillus niger strain to leach rare earth elements based on untargeted metabolomics analysis. *Chem. Eng. J.* **2023**, *475*, 146070. [CrossRef]
20. Zhou, H.; Wang, J.; Yu, X.; Kang, J.; Qiu, G.; Zhao, H.; Shen, L. Effective extraction of rare earth elements from ion-adsorption type rare earth ore by three bioleaching methods. *Sep. Purif. Technol.* **2024**, *330*, 125305. [CrossRef]
21. Wang, G.; Xu, J.; Ran, L.; Zhu, R.; Ling, B.; Liang, X.; Kang, S.; Wang, Y.; Wei, J.; Ma, L.; et al. A green and efficient technology to recover rare earth elements from weathering crusts. *Nat. Sustain.* **2023**, *6*, 81–92. [CrossRef]
22. Normile, D. A cleaner way to mine clean-energy mainstays. *Science* **2022**, *378*, 461. [CrossRef] [PubMed]
23. Prommer, H. Towards sustainable rare-earth-element mining. *Nat. Sustain.* **2023**, *6*, 13–14. [CrossRef]
24. Martens, E.; Prommer, H.; Dai, X.; Sun, J.; Breuer, P.; Fourie, A. Electrokinetic in situ leaching of gold from intact ore. *Hydrometallurgy* **2018**, *178*, 124–136. [CrossRef]
25. Martens, E.; Prommer, H.; Dai, X.; Wu, M.Z.; Sun, J.; Breuer, P.; Fourie, A. Feasibility of electrokinetic in situ leaching of gold. *Hydrometallurgy* **2018**, *175*, 70–78. [CrossRef]
26. Martens, E.; Prommer, H.; Sprocati, R.; Sun, J.; Dai, X.; Crane, R.; Jamieson, J.; Tong, P.O.; Rolle, M.; Fourie, A. Toward a more sustainable mining future with electrokinetic in situ leaching. *Sci. Adv.* **2021**, *7*, eabf9971. [CrossRef]
27. Ibsen, S.; Sonnenberg, A.; Schutt, C.; Mukthavaram, R.; Yeh, Y.; Ortac, I.; Manouchehri, S.; Kesari, S.; Esener, S.; Heller, M.J. Recovery of Drug Delivery Nanoparticles from Human Plasma Using an Electrokinetic Platform Technology. *Small* **2015**, *11*, 5088–5096. [CrossRef]
28. Xu, J.; Liu, C.; Hsu, P.C.; Zhao, J.; Wu, T.; Tang, J.; Liu, K.; Cui, Y. Remediation of heavy metal contaminated soil by asymmetrical alternating current electrochemistry. *Nat. Commun.* **2019**, *10*, 2440. [CrossRef] [PubMed]
29. Wen, D.; Fu, R.; Li, Q. Removal of inorganic contaminants in soil by electrokinetic remediation technologies: A review. *J. Hazard. Mater.* **2021**, *401*, 123345. [CrossRef]
30. Wang, Y.; Li, A.; Cui, C. Remediation of heavy metal-contaminated soils by electrokinetic technology: Mechanisms and applicability. *Chemosphere* **2020**, *265*, 129071. [CrossRef]
31. Glendinning, S.; Lamont-Black, J.; Jones, C.J.F.P. Treatment of sewage sludge using electrokinetic geosynthetics. *J. Hazard. Mater.* **2007**, *139*, 491–499. [CrossRef]
32. Jones, C.J.F.P.; Lamont-Black, J.; Glendinning, S. Electrokinetic geosynthetics in hydraulic applications. *Geotext. Geomembr.* **2011**, *29*, 381–390. [CrossRef]
33. Malekzadeh, M.; Lovisa, J.; Sivakugan, N. An Overview of Electrokinetic Consolidation of Soils. *Geotech. Geol. Eng.* **2016**, *34*, 759–776. [CrossRef]
34. Zhuang, Y. Large scale soft ground consolidation using electrokinetic geosynthetics. *Geotext. Geomembr.* **2021**, *49*, 757–770. [CrossRef]
35. Pires, C.M.G.; Ponte, H.A.; Grassi, M.T.; Ponte, M.J.J.S.; Ribeiro, A.B. Extracting light rare earth elements by applying electric field assisted mining technique. *Miner. Eng.* **2023**, *203*, 108354. [CrossRef]
36. Pires, C.M.G.; Ribeiro, A.B.; Mateus, E.P.; Ponte, H.A.; Ponte, M.J.J.S. Extraction of rare earth elements via electric field assisted mining applying deep eutectic solvents. *Sustain. Chem. Pharm.* **2022**, *26*, 100638. [CrossRef]
37. Pires, C.M.G.; Pereira, J.T.; Ribeiro, A.B.; Ponte, H.A.; Ponte, M.J.J.S. Optimization of Electric Field Assisted Mining Process Applied to Rare Earths in Soils. *Appl. Sci.* **2021**, *11*, 6316. [CrossRef]
38. Alshawabkeh, A.N.; Acar, Y.B. Removal of contaminants from soils by electrokinetics: A theoretical treatise. *J. Environ. Sci. Health Part A Environ. Sci. Eng. Toxicol.* **1992**, *27*, 1835–1861. [CrossRef]
39. Acar, Y.B.; Alshawabkeh, A.N. Principles of electrokinetic remediation. *Environ. Sci. Technol.* **1993**, *27*, 2638–2647. [CrossRef]
40. Alshawabkeh, A.N.; Acar, Y.B. Electrokinetic remediation. II: Theoretical model. *J. Geotech. Eng.* **1996**, *122*, 186–196. [CrossRef]
41. Pennathur, S.; Santiago, J.G. Electrokinetic Transport in Nanochannels. 1. Theory. *Anal. Chem.* **2005**, *77*, 6772–6781. [CrossRef] [PubMed]
42. Mattson, E.D.; Bowman, R.S.; Lindgren, E.R. Electrokinetic ion transport through unsaturated soil: 1. Theory, model development, and testing. *J. Contam. Hydrol.* **2002**, *54*, 99–120. [CrossRef] [PubMed]
43. Kong, X.; Jiang, J.; Lu, D.; Liu, Z.; Wu, J. Molecular Theory for Electrokinetic Transport in pH-Regulated Nanochannels. *J. Phys. Chem. Lett.* **2014**, *5*, 3015–3020. [CrossRef] [PubMed]
44. Liu, M.; Waugh, J.; Babu, S.K.; Spendelow, J.S.; Kang, Q. Numerical modeling of ion transport and adsorption in porous media: A pore-ccale study for capacitive deionization desalination. *Desalination* **2022**, *526*, 115520. [CrossRef]
45. Mou, D.; Lu, Y.; Chen, Y.; Wei, J.; Zhang, J. Simulation of dissolved-oxygen distribution in matrix particles during the aerobic composting process of sewage sludge with two-region model. *J. Clean. Prod.* **2023**, *428*, 139380. [CrossRef]
46. Zhang, X.; Cai, F.; Ma, F.; Reimus, P.; Qi, L.; Lu, D.; Reza, M.; Dai, Z. Investigating the role of na-bentonite colloids in facilitating sr transport in granite minerals through column experiments and modeling. *J. Hazard. Mater.* **2024**, *463*, 132851. [CrossRef]

47. Jabłońska, B. Optimization of Ni(Ii), Pb(Ii), and Zn(Ii) ion adsorption conditions on pliocene clays from post-mining waste. *Minerals* **2021**, *11*, 568. [CrossRef]
48. Mao, W.; Zhu, Y.; Ye, M.; Zhang, X.; Wu, J.; Yang, J. A new quasi-3-d model with a dual iterative coupling scheme for simulating unsaturated-saturated water flow and solute transport at a regional scale. *J. Hydrol.* **2021**, *602*, 126780. [CrossRef]
49. Pu, Q.; Yun, J.; Temkin, H.; Liu, S. Ion-enrichment and ion-depletion effect of nanochannel structures. *Nano Lett.* **2004**, *4*, 1099–11103. [CrossRef]
50. Li, J.; Peng, R.; Li, D. Effects of ion size, ion valence and pH of electrolyte solutions on EOF velocity in single nanochannels. *Anal. Chim. Acta* **2019**, *1059*, 68–79. [CrossRef]
51. Hu, J.S.; Chao, C.Y.H. Numerical study of electroosmotic (EO) flow in microfabricated EO pump with overlapped electrical double layer (EDL). *Int. J. Refrig.* **2007**, *30*, 290–298. [CrossRef]
52. Acar, Y.B.; Gale, R.J.; Alshawabkeh, A.N.; Marks, R.E.; Puppala, S.; Bricka, M.; Parker, R. Electrokinetic remediation: Basics and technology status. *J. Hazard. Mater.* **1995**, *40*, 117–137. [CrossRef]
53. Haynes, W.M. *CRC Handbook of Chemistry and Physics*; CRC Press: Boca Raton, FL, USA, 2016.
54. Alshameri, A.; He, H.; Xin, C.; Zhu, J.; Xinghu, W.; Zhu, R.; Wang, H. Understanding the role of natural clay minerals as effective adsorbents and alternative source of rare earth elements: Adsorption operative parameters. *Hydrometallurgy* **2019**, *185*, 149–161. [CrossRef]
55. Borst, A.M.; Smith, M.P.; Finch, A.A.; Estrade, G.; Villanova-de-Benavent, C.; Nason, P.; Marquis, E.; Horsburgh, N.J.; Goodenough, K.M.; Xu, C.; et al. Adsorption of rare earth elements in regolith-hosted clay deposits. *Nat. Commun.* **2020**, *11*, 4386. [CrossRef]
56. Díaz-Moreno, S.; Muñoz-Páez, A.; Chaboy, J. X-ray Absorption Spectroscopy (XAS) Study of the Hydration Structure of Yttrium(III) Cations in Liquid and Glassy States: Eight or Nine-Fold Coordination? *J. Phys. Chem. A* **2000**, *104*, 1278–1286. [CrossRef]